J. Fluid Mech. (2008), *vol.* 617, *pp.* 167–185.
doi:10.1017/S0022112008003868 Printed in the United Kingdom

Shape and stability of axisymmetric levitated viscous drops

JOHN R. LISTER[1]†, ALICE B. THOMPSON[2], ANTOINE PERRIOT[1] AND LAURENT DUCHEMIN[3]

[1]Department of Applied Mathematics and Theoretical Physics, Institute of Theoretical Geophysics, Wilberforce Road, Cambridge CB3 0WA, UK

[2]School of Mathematical Sciences, University of Nottingham, Nottingham NG7 2RD, UK

[3]IRPHE, 9, Rue F. Joliot-Curie, 13384 Marseille Cedex 13, France

(Received 19 October 2007 and in revised form 5 August 2008)

We consider levitation of an axisymmetric drop of molten glass above a spherical porous mould through which air is injected at a constant velocity. Owing to the viscosity contrast, the float height for a given shape is established on a much shorter time scale than the subsequent deformation of the drop under gravity, surface tension and the underlying lubrication pressure. Equilibrium shapes, in which an internal hydrostatic pressure is coupled to the external lubrication pressure through the total curvature and the Young–Laplace equation, are determined using a numerical continuation scheme. The set of solution branches is surprisingly complicated and shows a rich bifurcation structure in the parameter space ($Bo = \rho g V^{2/3}/\gamma$, $Ca = \mu_a v/\gamma$), where Bo is bond number and Ca is capillary number, ρ and V are the drop density and volume, γ the surface tension, μ_a the air viscosity and v the injection velocity. The linear stability of equilibria is determined using a boundary-integral representation for drop deformation that factors out the rapid vertical adjustment of the float height. The results give good agreement with time-dependent simulations. For sufficiently large Ca there are intervals of Bo for which there are no stable solutions and, as Ca increases, these intervals grow and merge. The region of stability decreases as the mould radius a_M increases with an approximate scaling $Ca \sim a_M^{-5}$, which imposes practical limitations on the use of this geometry for the manufacture of lenses.

1. Introduction

In a recent study, Duchemin, Lister & Lange (2005), hereafter referred to as DLL, investigated the axisymmetric equilibrium shapes of a viscous drop that is levitated above a spherical porous mould by a lubricating film of air injected through the mould. The study was motivated by an industrial process for the casting of glass lenses, which uses air-film levitation to avoid contact between a drop of molten glass and the mould, and thus achieves high surface quality in the finished product. There are two limitations to the process. The first is the existence of static 'brim' waves near the edge of the drop, where variations in the film thickness cause the drop to deviate from the shape of the mould. DLL adapted the analysis of Wilson & Jones (1983) to demonstrate that these brim waves are capillary ripples generated by the jump in curvature from that of the mould to that of the sessile upper surface. The scaling of the waves with the film capillary number, the mould slope and the capillary

† Email address for correspondence: lister@esc.cam.ac.uk

length were determined, and these are minimized for a given geometry by reducing the air injection rate as much as possible. The second limitation is an instability whereby, for some mould shapes, the air seems unable to escape the edge of the drop sufficiently rapidly, and so an air bubble accumulates under the centre of the drop, deforming it and eventually breaking through the drop's upper surface. This has been seen both experimentally and in Navier–Stokes simulations with the industrial finite-element code POLYFLOW (Lange 2002; figure 6 of DLL), but has not yet received a theoretical analysis. This is one of the purposes of this paper. The other is further exploration of the branches of equilibrium shapes.

The equilibrium shapes are determined from the Young–Laplace equation, which couples the hydrostatic pressure inside a stationary drop to the lubrication pressure in the air outside. In DLL, this equation was solved using a fourth-order adaptive Runge–Kutta shooting technique, which proved computationally delicate owing to the need to control spatially growing exponential perturbations on the lower surface. The curvature was also approximated by the two-dimensional curvature to avoid the coordinate singularity on the axis. While this seemed reasonable for large Bond-number flat-lying drops, the approximation was not evaluated and it is probable, as will be confirmed later, that the solution-branch structure was affected by it. The solution branches of DLL possessed two notable features. First, the branch structure (see figure 2) was much more convoluted than initially expected, owing to the possibility of solutions with large-amplitude oscillations on the base of the drop. If these solutions are discarded as almost certainly unstable, then the remaining more 'reasonable' solutions do not cover parameter space and the gaps are roughly coincident with the regions where time-dependent simulations show instability. This was suggestive, but not conclusive.

In this paper, we solve the Young–Laplace equation using the free continuation software AUTO97 (available at http://indy.cs.concordia.ca/auto/), which allows us much greater freedom to explore the bifurcation structure. We use the full axisymmetric curvature and show that this has a significant effect on the structure of solutions with large basal oscillations. The branch structure is still highly convoluted, however, and we illustrate some of the varied bifurcations. We also present a detailed linear stability analysis of the equilibrium shapes and show that the resultant predictions agree with time-dependent simulations. The stability analysis couples a boundary-integral representation of the flow inside the drop to the lubrication pressure outside the drop and an equation of quasi-steady vertical equilibrium. Throughout this paper, we consider axisymmetric perturbations to axisymmetric equilibria, since there is no indication in the industrial process that non-axisymmetric shapes are relevant.

We briefly note that drop levitation by air injection through a plane porous surface has been investigated by Goldshtik, Khanin & Ligai (1986) as a model for the well-known Leidenfrost phenomenon, whereby an evaporating drop is supported above a hot plate by a vapour film. In contrast to the larger viscous drops investigated here, Goldshtik *et al.* focused on water-like drops of not much more than capillary size. As a result, only a single monotonic branch of equilibrium solutions was found theoretically, and the self-sustained oscillations sometimes observed experimentally had inviscid dynamics.

1.1. *Dynamic regime*

Before embarking on detailed analysis, we briefly motivate the dynamical regime to be considered using parameters typical of the manufacturing process and some simple scaling estimates. The molten glass used for casting lenses has a typical viscosity

$\mu = 10^2$ Pa s, surface tension $\gamma = 0.3\,\mathrm{N\,m^{-1}}$ and density $\rho = 2400\,\mathrm{kg\,m^{-3}}$ (cf. Seward & Vascott 2006). The capillary length $l_c = (\gamma/\rho g)^{1/2}$ is thus about 3.6 mm, and a drop of typical radius $R_t = 5$ cm will have thickness of order $H = 2l_c = 7$ mm. Hot air of viscosity $\mu_a = 3 \times 10^{-5}$ Pa s and density $\rho_a = 0.6\,\mathrm{kg\,m^{-3}}$ is injected through the mould with Darcy velocity v of order $1\,\mathrm{cm\,s^{-1}}$.

It is apparent from the huge viscosity contrast that the time scale associated with deformation of the glass drop is likely to be much longer than that associated with the lubricating air film. This is readily confirmed using, for simplicity, the theory for the levitation of a rigid disk above a horizontal porous surface with injection (Hinch & Lemaitre 1994). (This is not quite the same problem, but has almost the same film thickness and allows estimation of the relevant time scales by straightforward analysis.) Consider a disk of thickness H and radius R levitated at a (uniform) height $h(t)$ above the surface. By mass conservation, the radial volume flux across radius r is $\pi r^2(v - \dot{h})$, where $\dot{h} = \mathrm{d}h/\mathrm{d}t$. From lubrication theory, this flux is driven by the radial gradient of a pressure $p(r,t) = 3\mu_a(v - \dot{h})(R_t^2 - r^2)/h^3$. The integral of this pressure over the bottom of the disk balances the weight and inertia $\pi R_t^2 H\rho(g + \ddot{h})$ of the disk. Finally, we obtain

$$\frac{\ddot{h}}{g} + \left(\frac{\dot{h}}{v} - 1\right)\left(\frac{h_0}{h}\right)^3 + 1 = 0, \tag{1.1}$$

where $h_0 = [3\mu_a v R_t^2/(\rho g H)]^{1/3}$ is the equilibrium float height. For the above parameters $h_0 = 0.25$ mm. Linearizing (1.1) about h_0 shows that vertical displacements are overdamped with a typical damping time $h_0/(3v) \approx 8$ ms.

A levitated drop has a curved lower surface, but h and h_0 can be thought of as typical values of the non-uniform film thickness. Vertical displacements are then governed by an equation similar to (1.1) and are damped on the same 8 ms time scale. On the other hand, a capillary-relaxation time scale for the molten glass drop is $\mu H/\gamma \approx 2$ s. This is much more than the vertical damping time, but comparable with the experimentally observed time scale of instability over some tens of seconds. We conclude that the drop rapidly achieves a quasi-equilibrium float height without significantly changing its shape, and then slowly changes its shape due to any mismatch between the lubrication pressure and that given by the Young–Laplace equation. This separation of time scales is a key feature of the analysis in the rest of the paper.

We close this preliminary section by noting that typical Reynolds numbers are estimated as $\rho_a v h_0/\mu_a = 0.05$ in the air film and $\rho\gamma H/\mu^2 = 5 \times 10^{-4}$ in the drop. It is thus appropriate to use the equations of lubrication theory in the air and of Stokes flow in the drop.

2. Governing equations

Consider a very viscous axisymmetric drop of viscosity μ, density ρ, surface tension γ and volume V that is being levitated above a porous mould with surface $z = f(r)$ by injection of air with viscosity μ_a at a Darcy velocity v (figure 1). The velocity v is assumed to be uniform, and not affected by the small variations in the air pressure p under the drop.

Let the drop have surface area A, given parametrically in terms of an arc length $s \in [0, L]$ by $\boldsymbol{x} = [\tilde{r}(s), \tilde{z}(s)]$ in cylindrical coordinates, where $s = 0$ at the bottom of the drop and $s = L$ at the top. The outward normal is given by $\boldsymbol{n}(s) = (\tilde{z}', -\tilde{r}')$, where

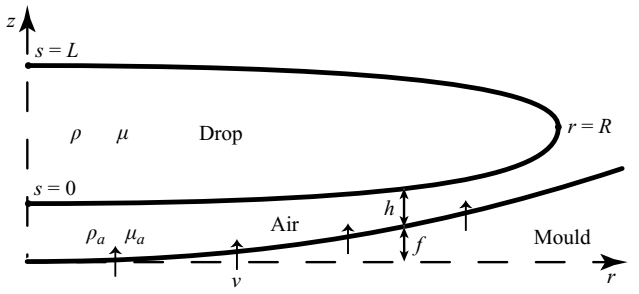

FIGURE 1. Sketch of the problem. Air is injected with Darcy velocity v through a porous mould with surface $z = f(r)$. A viscous drop of viscosity μ and density ρ with surface $(\tilde{r}, \tilde{z})$, $0 \leqslant s \leqslant L$, floats on a lubricating air film of viscosity μ_a and thickness $h = \tilde{z} - f(\tilde{r})$. The maximum radius is $r = R$.

primes denote $\mathrm{d}/\mathrm{d}s$, and the total curvature $\tilde{\kappa}$ is given by

$$\tilde{\kappa} = \frac{\mathrm{d}\psi}{\mathrm{d}s} + \frac{\sin\psi}{r}, \tag{2.1}$$

where

$$\psi = \tan^{-1}(\tilde{z}'/\tilde{r}') \tag{2.2}$$

is the angle between the tangent and the horizontal. The last term in (2.1) is the azimuthal curvature, which was neglected in DLL.

The normal-stress condition on the surface of the drop is the Young–Laplace equation

$$P - \rho g\tilde{z} = p + \gamma\tilde{\kappa}, \tag{2.3}$$

where p is the air pressure on the drop and the normal stress $\boldsymbol{n}\cdot\boldsymbol{\sigma}\cdot\boldsymbol{n}$ in the drop has been written as $\rho g\tilde{z} - P$ so that P represents the deviation from a hydrostatic state. The motion of the drop is thus driven by the distribution of the modified pressure P, which incorporates the effects of gravity, surface tension and the supporting lubrication pressure p. As usual in lubrication theory, the shear stress exerted by the air flow under the drop is very much less than p and can be neglected.

Let h denote the vertical thickness of the lubricating air film so that

$$h = \tilde{z} - f(\tilde{r}) \tag{2.4}$$

on the lower surface of the drop. As discussed earlier, deformation of the drop occurs much more slowly than establishment of a quasi-equilibrium float height, and thus $|\partial h/\partial t| \ll v$. Also, assuming that $|\partial h/\partial r| \ll 1$ and $|\partial f/\partial r| \ll 1$ in a shallow mould, we apply mass conservation and the lubrication approximation to obtain (DLL; Hinch & Lemaitre 1994)

$$-\frac{h^3}{12\mu_a}\frac{\partial p}{\partial r} = \frac{\pi r^2 v}{(2\pi r)}. \tag{2.5}$$

Thus

$$p(r) = 6\mu_a v \int_r^{\text{`}\infty\text{'}} \frac{r\,\mathrm{d}r}{h^3(r)}, \tag{2.6}$$

where '∞' denotes a point on the interface beyond which the gap h is sufficiently large that the air pressure can be considered to be uniform.

DLL took '∞' in (2.6) to be where $\tan\psi = 10$, arguing that p was negligible beyond this point. For convenience, we convert (2.6) to an integral with respect to arc length,

assume that (2.4) and (2.6) apply over the whole surface of the drop and take '∞' to be $s = L$. In § 3 we verify that, as expected, this simplifying assumption makes very little difference to the results since the strong dependence of the integrand on h means that the contribution from p on the upper surface is indeed negligible.

We make all lengths dimensionless with respect to the capillary length $l_c = (\gamma/\rho g)^{1/2}$ and pressures with respect to $\rho g l_c = \gamma/l_c$. We also introduce the two dimensionless parameters (Capillary and Bond numbers)

$$Ca = \frac{\mu_a v}{\gamma} \quad \text{and} \quad Bo = \frac{V^{2/3}}{l_c^2}. \tag{2.7}$$

In dimensionless form, (2.3) and (2.6) then reduce to

$$P(s) = \tilde{z}(s) + \tilde{\kappa}(s) + 6Ca \int_s^L \frac{\tilde{r}}{[\tilde{z} - f(\tilde{r})]^3} \frac{\mathrm{d}\tilde{r}}{\mathrm{d}s}\, \mathrm{d}s, \tag{2.8}$$

and $Bo^{3/2}$ is the dimensionless volume.

2.1. *Statics*

If P is uniform then the drop is in static equilibrium. The equation $\mathrm{d}P/\mathrm{d}s = 0$ can be rewritten with the help of (2.1), (2.2) and (2.8) as a set of four first-order ODEs:

$$\left.\begin{aligned} &\frac{\mathrm{d}\tilde{r}}{\mathrm{d}s} = \cos\psi, \frac{\mathrm{d}\tilde{z}}{\mathrm{d}s} = \sin\psi, \frac{\mathrm{d}\psi}{\mathrm{d}s} = k_1, \\ &\frac{\mathrm{d}k_1}{\mathrm{d}s} = \frac{6Ca\,\tilde{r}\cos\psi}{[\tilde{z} - f]^3} + \left(\frac{k_1 - k_2}{r}\right)\cos\psi - \sin\psi, \end{aligned}\right\} \tag{2.9a–d}$$

where k_1 is the two-dimensional curvature and $k_2 = (\sin\psi)/r$ is the azimuthal curvature. These equations are subject to the boundary conditions

$$\tilde{r}(0) = \psi(0) = 0, \quad \tilde{r}(L) = 0, \quad \psi(L) = \pi \tag{2.10}$$

and the volume constraint (which determines L)

$$\pi \int_0^L \tilde{r}^2 \sin\psi\, \mathrm{d}s = Bo^{3/2}. \tag{2.11}$$

2.2. *Dynamics*

If P is non-uniform then the Stokes flow in the drop can be determined from P using a boundary-integral representation (e.g. Rallison & Acrivos 1978; Lee & Leal 1982; Pozrikidis 1992). In particular, the velocity $\boldsymbol{u}$ on the surface of the drop, made dimensionless by γ/μ, is given by the solution of the singular integral equation

$$\tfrac{1}{2}\boldsymbol{u}(\boldsymbol{x}) = \int_A \boldsymbol{u}(\boldsymbol{y}) \cdot \boldsymbol{K} \cdot \boldsymbol{n}\, \mathrm{d}A_y + \int_A \boldsymbol{J} \cdot \boldsymbol{f}(\boldsymbol{y})\, \mathrm{d}A_y, \tag{2.12}$$

where

$$\boldsymbol{f} = -P\boldsymbol{n}, \tag{2.13}$$

$$\boldsymbol{J}(\boldsymbol{x}, \boldsymbol{y}) = \frac{1}{8\pi}\left(\frac{\boldsymbol{I}}{d} + \frac{\boldsymbol{dd}}{d^3}\right), \qquad \boldsymbol{K}(\boldsymbol{x}, \boldsymbol{y}) = -\frac{3}{4\pi}\frac{\boldsymbol{ddd}}{d^5} \quad \text{and} \quad \boldsymbol{d} = \boldsymbol{x} - \boldsymbol{y}. \tag{2.14}$$

Equation (2.12) has a null eigenvector $\boldsymbol{u} = \hat{\boldsymbol{z}}$, where $\hat{\boldsymbol{z}}$ is the unit vertical vector, and the corresponding solubility condition is

$$\hat{\boldsymbol{z}} \cdot \int_A \boldsymbol{f} \, \mathrm{d}A = 0. \tag{2.15}$$

Equation (2.15) is the condition that there is no net vertical force on the drop and can be shown, from (2.3), (2.13) and $\tilde{\kappa} = \nabla \cdot \boldsymbol{n}$, to be equivalent to a balance between the weight ($\rho g V$ or $Bo^{3/2}$) of the drop and the net vertical force from the lubrication pressure p. This balance reflects the assumption that the drop establishes a quasi-equilibrium float height on a time scale much shorter than that of deformation.

The maintenance of an equilibrium float height as the drop deforms determines what multiple of the null eigenvector $\hat{\boldsymbol{z}}$ must be added to a solution of (2.12). The evolution of the drop is thus determined by (2.8) and (2.12)–(2.15).

3. Static equilibria

Equations (2.9)–(2.11) were solved using the continuation software AUTO97. The starting point was a spherical drop of a given volume in the absence of both gravity and lubrication pressure. The effects of gravity and the lubrication pressure were then increased by continuation until (2.9*d*) was satisfied, giving an equilibrium solution for particular values of Bo and Ca. A branch of equilibrium solutions can then be explored by continuation in either Bo or Ca. The results discussed later are mainly for the spherical mould considered by Lange (2002) and DLL, namely

$$f(r) = a_M - \left(a_M^2 - r^2\right)^{1/2}, \tag{3.1}$$

with $a_M = 50$. The effect of the mould radius a_M is considered in § 3.4.

3.1. *The effect of full curvature*

We begin by testing the continuation method against the results of DLL, which were obtained by shooting, and by evaluating the effect of the azimuthal curvature k_2. In figure 2 we show the solution branches obtained by continuation for $Ca \approx 4 \times 10^{-5}$ to both the system (2.9)–(2.11) and the system solved by DLL in which k_2 is omitted from (2.9*d*). The branch structure obtained for the system with only the two-dimensional curvature agrees with, and even extends, that shown in figure 2 of DLL, thus validating the AUTO code.

The branch structure obtained with the full curvature has the following features in common with that obtained from the two-dimensional approximation: (1) For many values of Bo there are multiple solutions. For example, in figure 3 we show five different equilibrium shapes for the same parameters $Bo = 100$, $Ca = 3.59 \times 10^{-5}$. (2) For many values of Bo the solutions with the smallest radius R lie close to that for a sessile drop with 180° contact angle with the mould (the limit as $Ca \to 0$). These solutions correspond to 'reasonable' shapes in which the lower surface of the drop approximately follows the shape of the mould. (3) The solutions with the larger values of R lie on extensions of the branches well above the trend of the sessile curve. These solutions correspond to more exotic shapes in which there are large-amplitude waves on the lower surface of the drop (cf. figure 3 of DLL and figure 3 here). Sufficiently far along the branch extensions, the waves pierce the upper surface; such self-intersecting shapes are clearly non-physical despite satisfying (2.9)–(2.11). (4) There are two gaps around $Bo = 25$ and $Bo = 75$ where there is no solution branch close to the trend of the sessile solution.

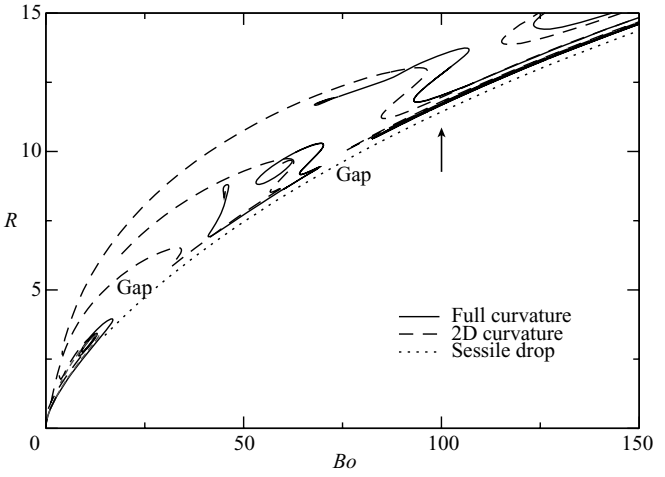

FIGURE 2. Solution branches at $Ca = 3.59 \times 10^{-5}$ with the full curvature (solid) and the two-dimensional approximation of DLL (dashed). The lowest parts of the solution branches lie close to the solution for a sessile drop with 180° contact angle (dotted), but there are two gaps around $Bo = 25$ and 75 where there are no solutions near the sessile curve. The full-curvature solutions for $Bo = 100$ (arrow) are shown in figure 3.

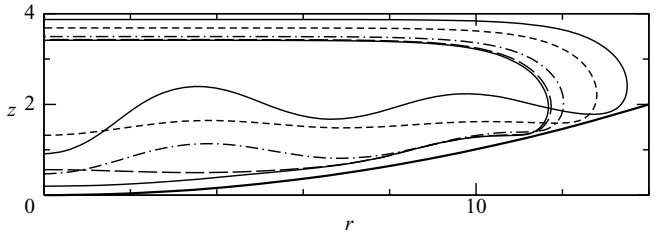

FIGURE 3. Five different equilibrium solutions with the full curvature for $Bo = 100$ and $Ca = 3.59 \times 10^{-5}$. The shape with the smallest radius R is stable. The other four, more elevated and exotic shapes, are unstable (see § 4).

The most obvious differences between the solution branches for the full curvature and for the two-dimensional curvature are in the form of the large-R extensions of the branches away from the sessile trend. As we shall see in § 4, these more exotic solutions are unstable anyway and hence these differences are not of much consequence. A more important difference is that the gaps in the 'reasonable' solutions along the sessile trend occur at larger Bo with the full curvature. For example, at $Ca = 3.59 \times 10^{-5}$ there is a gap $16.9 < Bo < 41.0$ with the full curvature and $13.5 < Bo < 31.6$ with the two-dimensional curvature. These gaps are regions where there are no stable axisymmetric solutions and hence it is not possible to cast a lens with these parameters using the levitation process.

3.2. *The effect of the lubrication approximation*

In using (2.9*d*) over the entire surface for simplicity, we have assumed that it does not matter much what approximation is used for p on the upper surface since p is negligible there. In order to test this, we compared the solutions of (2.9)–(2.11) with two other approximations. First, we replaced $\cos\psi$ by 1 in the first term of (2.9*d*). This is equivalent to replacing $\partial p/\partial r$ by $\partial p/\partial s$ in (2.5) and noting that $\psi \approx 0$ and $r \approx s$

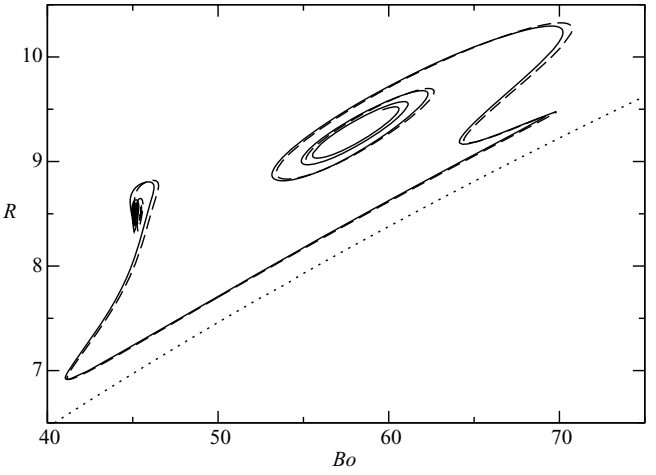

FIGURE 4. Detail of a solution branch at $Ca = 3.59 \times 10^{-5}$ for the alternative lubrication approximations in which (2.9*d*) is modified as described in § 3.2. (i) $\cos\psi \mapsto 1$ (dashed) and (ii) $\cos\psi \mapsto 0$ if $\cos\psi < 0$ (solid). The unmodified (2.9*d*) gives a branch that is indistinguishable in this figure from alternative (ii) (see also figures 2 and 6*b*) The solution curves lie above that for a sessile drop (dotted).

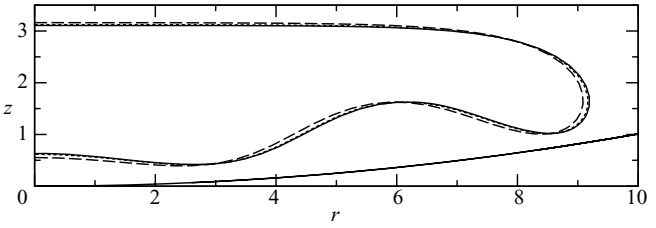

FIGURE 5. The equilibrium shape with the smallest R for $Ca = 10^{-3}$ and $Bo = 60$ with (2.9*d*) unmodified (solid), with $\cos\psi \mapsto 1$ (dashed) and with $\cos\psi \mapsto 0$ if $\cos\psi < 0$ (dotted). There is very little difference between the three approximations, even though the gap thickness is quite large for this Ca (see § 3.2 for discussion). The shape is stable (see figure 11*b*).

in the lubricating film, though not on the upper surface. Second, we replaced $\cos\psi$ by 0 in the first term of (2.9*d*) when $\cos\psi < 0$. This is equivalent to setting $p = 0$ on the upper surface of the drop, or taking '∞' to be the point of maximum radius rather than $s = L$. As shown in figures 4 and 5, these alternative approximations give essentially the same solution shapes and branch structure as the original approximation, and so we will use (2.9*d*) from now on.

3.3. *Bifurcations in the branch structure*

It is clear from figures 2 and 4 that the solution branches are quite complicated, even at a fixed value of Ca. In figure 6, we show the branch structure for a number of values of Ca, which gives an impression of some of the many bifurcations that occur as Ca increases. An alternative view is provided in figure 7 by a plot in the (Bo, Ca) plane of the location of some of the solution fold points. It is worth noting again that only the solutions close to the sessile trend prove to be stable. Nevertheless, it is necessary to understand something about the branch and bifurcation structures to know when such solutions might exist. The following features can be discerned in figures 6 and 7: (1) In a number of places there are two or more branches very close

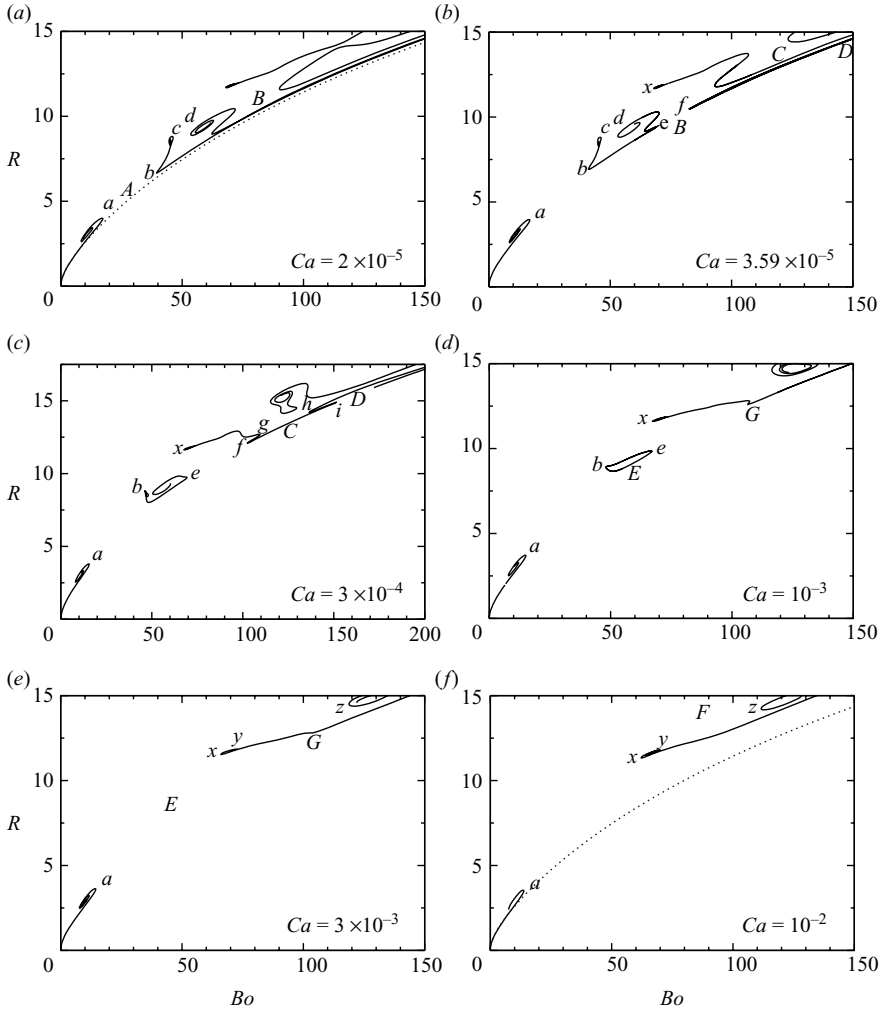

FIGURE 6. Solution branches at (*a*) $Ca = 2 \times 10^{-5}$, (*b*) 3.59×10^{-5}, (*c*) 3×10^{-4}, (*d*) 10^{-3}, (*e*) 3×10^{-3} and (*f*) 10^{-2}. Letters *a–i*, *x–z* denote the fold points plotted in figure 7, and *A–H* denote some of the bifurcations in the structure of the branches. The sessile solution is shown dotted in (*a*) and (*f*).

and parallel to each other along the sessile trend. The main difference between the corresponding shapes is in the curvature in the middle of the lower surface (cf. the lowest two shapes in figure 3). As Ca increases, these nearly parallel branches can touch and reconnect to leave a gap in the branch structure with a fold point on either side. This process can be seen at points *A–D*. For the cases *A*, *B* and *D*, this creates a gap in solutions along the sessile trend. (2) In a number of places solution branches terminate in a spiral structure. At points *E* and *F* the spirals at each end of a branch touch to form a closed loop (isola) of solutions, which shrinks and disappears as Ca increases further. At *E* the gaps created near $Bo = 25$ and $Bo = 70$ at *A* and *B* merge to form a large gap along the sessile trend that extends over $15 \leqslant Bo \leqslant 100$. (3) The reconnections *B*, *C* and *D* create kinks in the branch structure, which can be seen

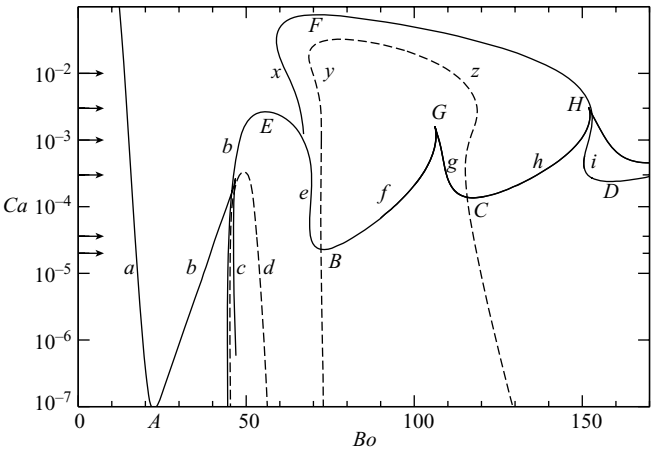

FIGURE 7. The variation with Ca of the fold points a–i and x–z shown at particular values of Ca (arrows) in figure 6. Folds appear by the collision of two branches at A–D; the dashed curves are folds that touch to form isolas, which subsequently shrink and disappear at E and F; kinks in solution branches disappear in cusp catastrophes at G and H.

in figure 6(c). The kinks fg and hi pull straight at G and H in cusp catastrophes, whereby three solutions become one.

The stability of solutions near these bifurcations will be described in § 4.

3.4. *Variation with the mould radius a_M*

We performed a brief exploration of the effect of varying the mould radius a_M in (3.1). The qualitative behaviour for $a_M = 100$ and 200 is very similar to that described above for $a_M = 50$, though there are differences in the detailed shape of the branches for the 'exotic' solutions with large-amplitude waves on the lower surface. Collision of branches close to the sessile trend still creates gaps and kinks in the branch structure, as described in § 3.3; the variation of some of the corresponding fold points is shown in figure 8. The first gap in the sessile trend (bifurcation A) appears near $Bo = 22$ for all three values of a_M; the width of the first gap is almost independent of a_M if Ca is scaled by a_M^{-5}. The appearance of gaps at B, C and D for $a_M = 50$ has analogues for $a_M = 100$ and 200, but there is more variation in the critical Bo for these gaps and there is only an approximate scaling of Ca with a_M^{-5}. Moreover, the fold structure for $a_M = 200$ has some features that do not have analogues for $a_M = 50$.

4. Stability

4.1. *Theory*

Consider the evolution of an equilibrium shape $\tilde{\boldsymbol{x}}(s)$ under an infinitesimal perturbation

$$\tilde{\boldsymbol{x}}(s) \to \tilde{\boldsymbol{x}}(s) + \boldsymbol{\delta}(s) \tag{4.1}$$

to the interfacial position. In order to represent a physically realizable perturbation, $\boldsymbol{\delta}$ should be such that both the volume of the drop and the vertical-force balance (2.15) are preserved. The application of these constraints is discussed further below.

By linearizing (2.8) about equilibrium, we can obtain the perturbation ΔP to the modified pressure P on the drop in the form

$$-\Delta P\, \boldsymbol{n} = \boldsymbol{F}[\delta], \tag{4.2}$$

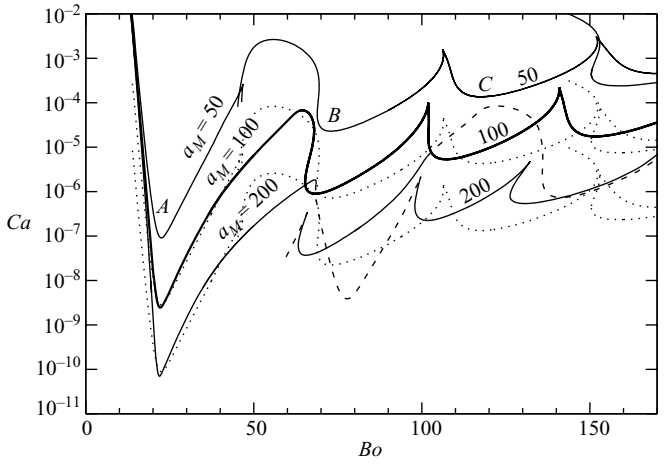

FIGURE 8. The variation of some of the fold points for mould radius $a_M = 50$, 100 and 200. Some of the fold structures for $a_M = 200$ have no analogue when $a_M = 50$ or 100 and are shown dashed. The dotted curves are the results for $a_M = 50$ reduced by factors of 32 and 1024 to show the approximate scaling $Ca \sim a_M^{-5}$.

where $\boldsymbol{F}[\delta]$ is a linear functional of δ; the detailed calculation is described in the Appendix. The operator $\boldsymbol{F}$ is non-local due to the integration involved in the lubrication pressure. Since P is uniform in equilibrium, it produces no flow, and thus the linearized flow is driven by $\boldsymbol{F}[\delta]$ acting on the unperturbed shape.

The vertical-force balance (2.15) is imposed by subtracting an appropriate vertical translation from δ. Accordingly, we define a projection operator $\boldsymbol{P}$ by

$$\boldsymbol{P}[\delta] = \delta - \hat{z}\left(\hat{z}\cdot\int \boldsymbol{F}[\delta]\,\mathrm{d}A\right)\Big/\left(\hat{z}\cdot\int \boldsymbol{F}[\hat{z}]\,\mathrm{d}A\right) \tag{4.3}$$

so that $\boldsymbol{FP}[\delta]$ satisfies (2.15). Thus $\boldsymbol{P}$ projects a general perturbation δ onto one that satisfies the vertical-force balance. It also follows from (4.3) that $\boldsymbol{P}[\hat{z}] = \boldsymbol{0}$.

The interfacial velocity $\boldsymbol{u}$ driven by the force distribution

$$f = \boldsymbol{FP}[\delta] \tag{4.4}$$

is obtained from the boundary-integral representation (2.12). The linearized equation is of the form

$$\boldsymbol{A}[\boldsymbol{u}] = \boldsymbol{J}[f], \tag{4.5}$$

where the operator $\boldsymbol{A} = \frac{1}{2}\boldsymbol{I} - \boldsymbol{K}$ is singular with null eigenvector $\hat{z}$, and $\boldsymbol{J}$ and $\boldsymbol{K}$ are the obvious integral operators over the unperturbed shape. Since f satisfies the solubility condition (2.15) by construction, (4.5) can be inverted to give

$$\boldsymbol{u} = \boldsymbol{A}^{-1}\boldsymbol{J}[f] + k\hat{z}\,. \tag{4.6}$$

The vertical velocity $k\hat{z}$ in (4.6) is determined by applying the projection operator $\boldsymbol{P}$ to $\boldsymbol{u}$ so that the vertical-force balance (2.15) continues to be satisfied as the interface moves under the kinematic boundary condition $\dot{\boldsymbol{\delta}} = \boldsymbol{u}$, where the dot denotes $\mathrm{d}/\mathrm{d}t$.

Finally, we note that the tangential components of $\boldsymbol{u}$ and $\boldsymbol{\delta}$ do not change the shape, and define $\delta = \boldsymbol{\delta}\cdot\boldsymbol{n}$. Thus

$$\dot{\delta} = \boldsymbol{n}\cdot\boldsymbol{PA}^{-1}\boldsymbol{JFP}[\delta\boldsymbol{n}] \quad \text{or} \quad \dot{\delta} = \boldsymbol{S}[\delta]. \tag{4.7}$$

The operator $\boldsymbol{S}$ has two zero eigenvalues: $\boldsymbol{P}[\hat{z}] = \boldsymbol{0}$ from (4.3); $\boldsymbol{J}[\boldsymbol{n}] = \boldsymbol{0}$ since a uniform pressure gives no flow. Hence $\boldsymbol{\delta} = \hat{z}$ and $\boldsymbol{\delta} = (\boldsymbol{FP})^{-1}[\boldsymbol{n}]$ both give $\boldsymbol{S}[\delta] = 0$. Now $\hat{z}$ is a vertical translation and $(\boldsymbol{FP})^{-1}[\boldsymbol{n}]$ is the perturbation that gives an equilibrium (constant P) drop of a slightly different volume. So the two null eigenvalues correspond to perturbations that do not conserve the vertical-force balance and the volume. The remaining eigenvalues correspond to eigenfunctions $\delta(s)$ that do conserve the vertical-force balance and volume, and are thus physically realizable. These non-trivial eigenvalues and eigenfunctions determine the dynamics and stability of the drop under small perturbations.

4.2. *Numerical calculation of stability*

The equilibrium shapes returned by AUTO97 are represented by the values of $[\tilde{r}(s), \tilde{z}(s)]$ at N unevenly spaced gridpoints, where typically $N = 100$ and the spacing is adapted as part of the continuation procedure to give good resolution of regions of rapidly changing curvature. In the stability calculation, the perturbation δ is also represented by the values at these gridpoints, and $\boldsymbol{S}$ becomes an $N \times N$ matrix with $N - 2$ dynamically significant eigenvalues. In order to calculate $\boldsymbol{S}$, both the equilibrium shape and the perturbation are interpolated with quintic splines, from which normals and curvatures can be calculated with high accuracy.

As usual, the azimuthal integrations of the kernels in (2.12) were performed analytically in terms of elliptic integrals using the formulae given in Lee & Leal (1982). The leading-order logarithmic singularity in the arc-length integration of the $\boldsymbol{J}$-integral was subtracted and integrated analytically. The remaining integrations in the discrete representations of the operators $\boldsymbol{J}$ and $\boldsymbol{K}$, the integration involved in the contribution of the lubrication pressure to $\boldsymbol{F}$ and the integration in (4.3) for $\boldsymbol{P}$ were all performed using a seven-point Gaussian scheme.

Since they relate vectors at the N gridpoints, $\boldsymbol{F}$, $\boldsymbol{P}$, $\boldsymbol{J}$, $\boldsymbol{K}$ and $\boldsymbol{A}$ are all represented as $2N \times 2N$ matrices. The matrix representation of $\boldsymbol{S}$ is readily constructed from these matrices, $\boldsymbol{n}$ and (4.7). The eigenvalues and eigenvectors of $\boldsymbol{S}$ are found using NAG subroutines.

4.3. *Comparison with time-dependent simulations*

The stability calculation described above can be tested by comparison with the observed decay rate towards equilibrium in a time-dependent simulation of the evolution of a drop with parameters such that the equilibrium shape is stable.

The time-dependent simulations were performed using a similar numerical method to the stability calculation (though the two codes were written largely independently and by different authors). The time-dependent code solves (2.12)–(2.15), (2.8) and the kinematic condition $\dot{\boldsymbol{x}} = \boldsymbol{u}$. The interface is represented by N gridpoints, with $N \approx 100$, and is interpolated using a cubic spline. The integration of the kernel functions $\boldsymbol{J}$ and $\boldsymbol{K}$ was performed as above to transform (2.12) into a matrix equation for the values of $\boldsymbol{u}$ at the gridpoints. The (near) singularity in the matrix equation, caused by the (nearly) null eigenvector $\boldsymbol{u} = \hat{z}$, was suppressed using singular value decomposition to find the interfacial velocity to within a vertical translation. The interface was advanced using forward-Euler time stepping with the normal velocity. A vertical translation to the new float height was added, with the magnitude determined from a bisection search on (2.15). A tangential redistribution of points with a suitable weighting function was used to maintain good resolution, in particular of the rapid decrease in the lubrication pressure near the edge of the drop.

In figure 9, we show two examples of decay of the interfacial velocity towards equilibrium for $Bo = 55$, $Ca = 10^{-7}$ and for $Bo = 50$, $Ca = 10^{-4}$. The initial shape in

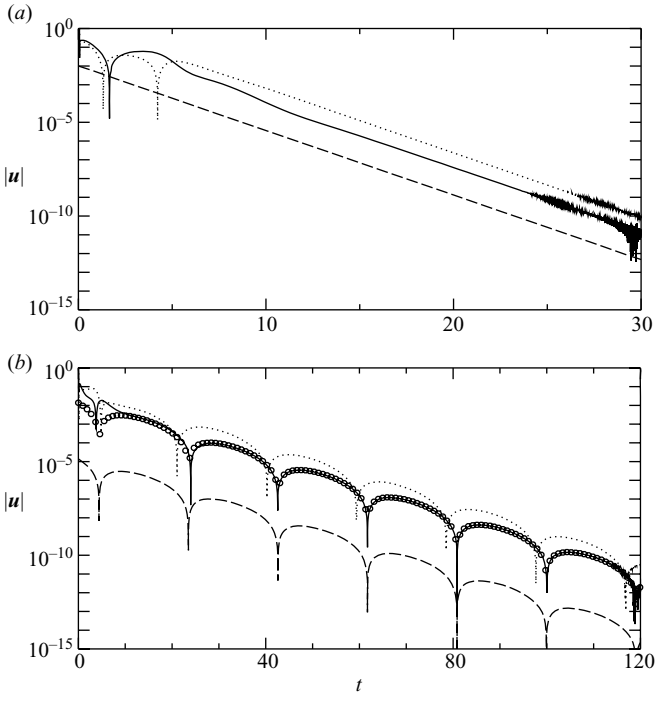

FIGURE 9. Time-dependent decay of $|\boldsymbol{u}|$ at the top (solid) and bottom (dotted) of a perturbed drop. (*a*) $Bo = 55$, $Ca = 10^{-7}$. The dashed line is the function $0.01\exp(-0.792t)$. (*b*) $Bo = 50$, $Ca = 10^{-4}$. The circles lie on the fitted function $0.021\exp(-0.176t)|\cos(0.164t + 0.85)|$ (also shown dashed after multiplying by 10^{-3}). Note that the velocities at the top and bottom of the drop are not in phase.

each case was a rescaling of an approximate equilibrium for a different value of Bo. The decay was characterized by the velocity at $r = 0$ on the top and bottom of the drop. The initial perturbation is a mixture of eigenmodes, but after a while the perturbation becomes dominated by the most slowly decaying mode. For $Bo = 55$ and $Ca = 10^{-7}$ the decay becomes monotonic with a real decay rate $\sigma = -0.792$. For $Bo = 50$ and $Ca = 10^{-4}$ the decay is oscillatory with a complex decay rate $\sigma = -0.176 \pm 0.164\mathrm{i}$. These values are in good agreement with the predictions of the numerical stability analysis, which gives $\sigma = -0.799$ and $-0.181 \pm 0.167\mathrm{i}$, respectively.

There is also good agreement between the normal velocity $\boldsymbol{u}\cdot\boldsymbol{n}$ of the time-dependent calculation and the real part of the eigensolution δ from the stability analysis. As shown in figure 10, the oscillatory decay for $Ca = 10^{-4}$ is characterized by the outward propagation of waves on the underside of the drop, which are driven by the variations in the lubrication pressure. There are also outward propagating waves on the upper surface, but of lower amplitude and with a phase lag. This suggests that the waves on the upper surface are driven by the deformation of the lower surface and reduced by capillary and gravitational levelling. The displacement and normal velocity are almost zero at the outer 'nip' where the lubricating air gap is narrowest near $r = 7.3$, since the vertical-force balance (2.15) is very sensitive to the gap thickness in this region. The outward and inward motions of the rim of the drop beyond the nip in $r > 7.3$ correspond to spreading and contraction of the drop as air accumulates and discharges from the gap beneath the drop.

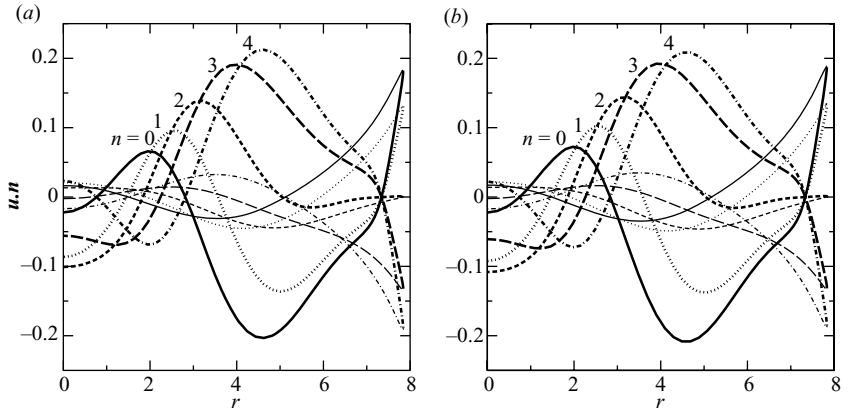

FIGURE 10. Profiles of the normal velocity for the oscillatory decay at $Bo = 50$ and $Ca = 10^{-4}$ over half an oscillation. The decay $\exp(-0.181t)$ is suppressed. The larger velocities (bold) are on the lower surface. (*a*) $\boldsymbol{u}\cdot\boldsymbol{n}\exp(0.181t)$ from the time-dependent simulation for $t = 40+(n\pi/4)/0.167$, $n = 0, \ldots, 4$. (*b*) $\mathrm{Re}(\delta e^{i\phi})$ from the linear stability calculation for $\phi = n\pi/4$. The (arbitrary) amplitude of the least stable eigenmode δ was chosen to match the simulation in (*a*).

4.4. *Stability of branches*

In figure 3 we showed five equilibrium shapes for $Bo = 100$ and $Ca = 3.59 \times 10^{-5}$. The least stable eigenvalue for each shape is real and given, in the order of increasing maximum radius R, by $\sigma = -0.41, 0.33, 0.84, 1.92$ and 2.37, respectively. Thus only the smallest-radius lowest-lying shape is stable, and the others are all unstable. The equilibrium shape for $Bo = 60$ and $Ca = 10^{-3}$ shown in figure 5 is stable with $\sigma = -0.054 + 0.146\mathrm{i}$, but the other equilibrium, with the larger value of R at $Bo = 60$ on the isola in figure 6(*d*), is unstable with $\sigma = 0.198$. These examples suggest a simple rule of thumb that the solution with the smallest value of R is stable and others, if they exist, are unstable. Unfortunately, this is an oversimplification, though it does appear to be true that only the solution with the smallest value of R can be stable.

The first point to note is that there is always a neutrally stable eigenmode where a solution branch has a fold point with respect to Bo. This can be argued from the canonical form of a saddle-node bifurcation or, more simply, by noting that the deformation from an equilibrium on the lower part of the branch to the equal-volume equilibrium on the upper part is clearly a neutrally stable (finite-amplitude) perturbation. As the fold is approached, this perturbation becomes infinitesimal and corresponds to a neutrally stable linear eigenmode. A similar argument shows that this eigenmode exchanges stability round the fold.

An example of loss of stability at a fold is shown in figure 11(*a*), which plots the least stable eigenvalue near the fold *a* for $Ca = 10^{-3}$ (see figure 6*d*). The lower-R part of the branch, which connects *a* to the origin, is stable and increasingly stable as $Bo \to 0$ and the drop becomes small and nearly spherical. The higher-R part leading towards the spiral is unstable (though the solution of (2.9)–(2.11) becomes self-intersecting before the spiral, and it then makes no sense to discuss the dynamics). Similar behaviour is found near *a* for other values of Ca, so that the entire region to the left of *a* in figure 7 contains a single stable solution.

Secondly, at all the folds we have examined, the neutral mode becomes unstable as the fold is rounded in the direction of increasing R. It does not follow that the

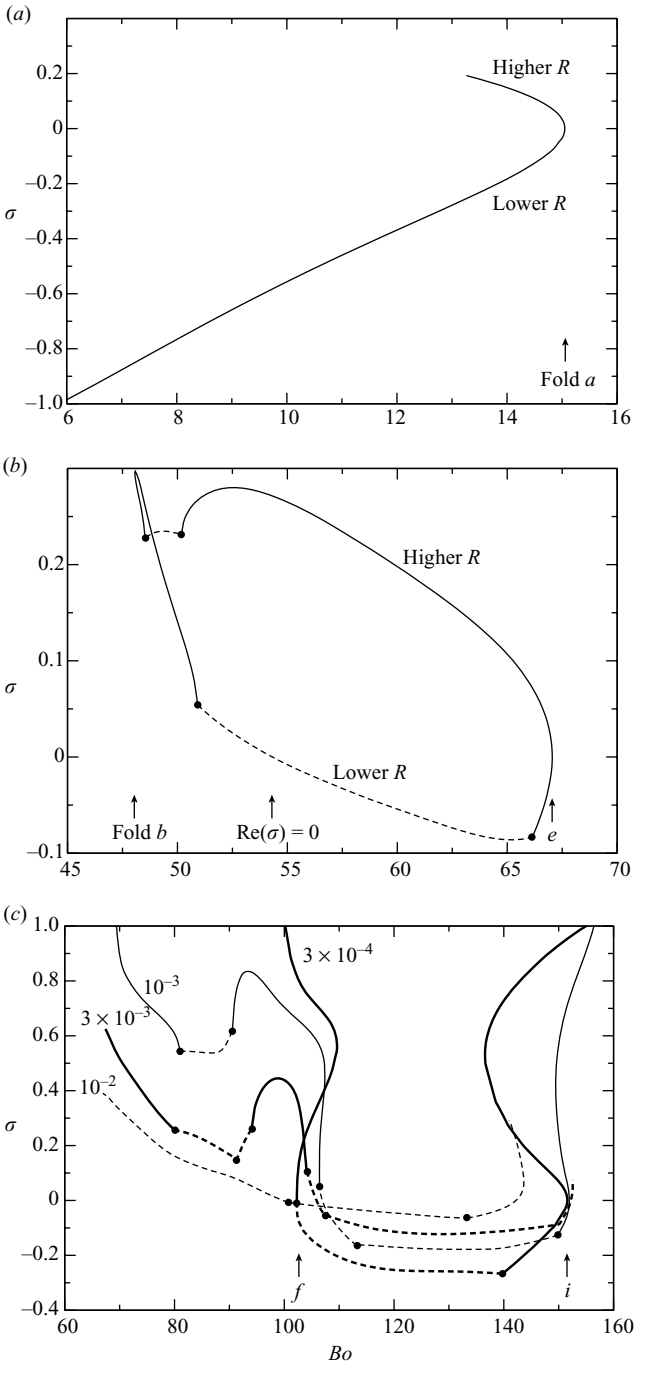

FIGURE 11. The least stable eigenvalue σ, or its real part, as a function of Bo for different Ca (see figure 6 for the shape of the branches). Dashed curves denote a complex eigenvalue, and the dots denote places where eigenvalues cross. (*a*) $Ca = 10^{-3}$. The solution along the sessile trend from the origin is stable and becomes unstable at the fold a where $Bo = 15.1$. The solution with larger R is unstable, and is self-intersecting for $Bo < 13.2$. (*b*) $Ca = 10^{-3}$. The isola of equilibria exists in $48.1 \leqslant Bo \leqslant 67.0$ but the lower part of the loop is only stable in $54.3 \leqslant Bo \leqslant 67.0$. (*c*) $Ca = 3 \times 10^{-4}$, 10^{-3}, 3×10^{-3} and 10^{-2}. The region between folds f and i at $Ca = 3 \times 10^{-4}$ is stable. As Ca increases to 10^{-2} the region of stability decreases to $99.8 \leqslant Bo \leqslant 142.3$ and becomes less stable.

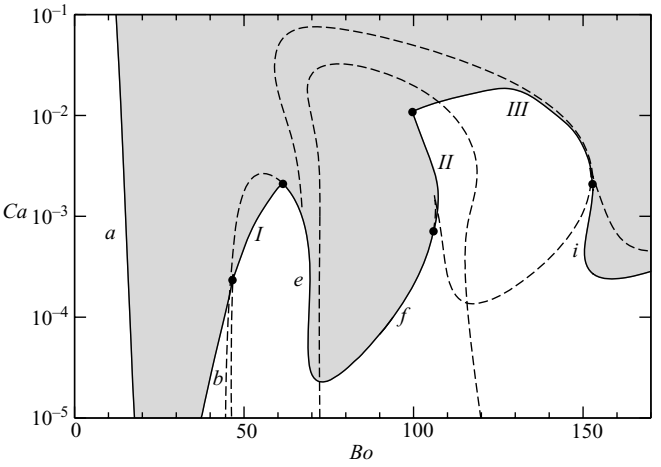

FIGURE 12. The critical Ca below which there is one stable equilibrium and above which (shaded) there are no stable equilibria. Most of this boundary (solid line) coincides with the folds a, b, e, f and i; the segments I–III correspond to neutral modes that are not at a fold (figure 11b, c). Some of the other folds are shown (dashed lines) to aid comparison with figure 7.

solution with smaller R is stable, since there may be at least one unstable mode before the fold is even reached. An example of this is shown in figure 11(b), which plots the least stable eigenvalue around the isola of equilibria for $Ca = 10^{-3}$. Though the isola extends between the folds b and e over $48.1 \leqslant Bo \leqslant 67.0$, the lower part of the loop is stable only in $54.3 \leqslant Bo \leqslant 67.0$. There is a neutrally stable mode at the fold b, which is stable along the lower part of the loop, but there is also at least one unstable mode in $48.1 \leqslant Bo \leqslant 54.3$. Similar behaviour is found for other values of Ca where the isola exists, and so a part of the region between b and e in figure 7 contains no stable solutions. Figure 11(b) also shows that different modes can become the most unstable as Bo varies, and that some values give oscillatory behaviour and others monotonic.

The other major region in the (Bo, Ca) plane where loss of stability is not simply given by the neutral mode at a fold is associated with the disappearance of the kinks at G and H as Ca increases. As shown in figure 11(c), for $Ca = 3 \times 10^{-4}$ the folds f and i are neutrally stable and the solution branch between them is stable. For $Ca = 10^{-3}$ the fold f is slightly unstable to another mode, as also is fold i for $Ca = 3 \times 10^{-3}$. Thus the folds become unstable slightly before they disappear at G and H, and the branch between them becomes less stable. This trend continues after G and H so that for $Ca = 10^{-2}$ the range of stability decreases to $99.8 \leqslant Bo \leqslant 142.3$, and for $Ca > 2 \times 10^{-2}$ no part of the branch is stable.

The stability results are summarized in figure 12. Below a critical Ca there is one stable equilibrium and above it there is none. Most of the critical curve coincides with the folds a, b, e, f and i of figure 7, the exceptions being those just described with reference to figures 11(b) and 11(c).

5. Concluding remarks

We have examined the shape and stability of an axisymmetric viscous drop levitated above a mould by a lubricating air film. Though this appears to be a simple physical

problem, the static solution structure and the dynamic stability are surprisingly complicated. The source of these complications is almost certainly the presence of capillary waves on the lower surface of the drop, which are required to match the curvature of a nearly sessile upper surface to that imposed by the mould on the lower surface.

We can gain some understanding of the effect of these waves in the limit $Ca \ll 1$. In this limit, DLL showed that the lubricating film thickness h obeys the third-order differential equation

$$h^3(h''' + f') = 6Ca\, r, \tag{5.1}$$

which supports a series of nips and lobes near the edge of the drop that decay exponentially towards a uniform thickness in the middle (cf. Wilson & Jones 1983). Solutions to (5.1) depend asymptotically on the small parameter

$$\delta = \left\{6Ca[f'(R_t)]^5 R_t\right\}^{1/3}, \tag{5.2}$$

where R_t is the dimensionless contact radius of the sessile solution with no air injection. The width of the first lobe scales like

$$\delta^{3/10} l_c / f'(R_t) = \left\{6Ca R_t / [f'(R_t)]^5\right\}^{1/10} l_c, \tag{5.3}$$

and subsequent nips and lobes have almost identical scalings (see Appendix A of DLL). This is the probable explanation of the approximate scaling $Ca \sim a_M^{-5}$ of some of the structures in figure 8 since $f'(R_t)$ is approximately proportional to a_M^{-1} when $a_M \gg R_t$. The boundary condition $h' = 0$ at $r = 0$ is sensitive both to the phase of the exponentially small oscillatory solutions of (5.1) and to the need to suppress an exponentially growing solution. This casts some light on the variations in figure 7 with Bo and on the existence of very similar equilibrium shapes that differ slightly in the middle (see figure 3). However, it falls short of a complete explanation of the complexity seen in figures 6 and 7. This complexity, and that of the crossing eigenmodes in figure 11, suggests that careful numerical solution will remain necessary for accurate quantitative predictions.

We find that a continuation method is a very effective way to determine the branches of equilibrium solutions from the governing ODEs and to explore their dependence on parameters. In particular, it is better adapted to deal with the oscillatory variations on the lower surface than the shooting method of DLL. The approximation of the full axisymmetric curvature by the two-dimensional curvature does not greatly affect the shape of drops close to the sessile trend. However, it does have a significant effect on the range of drop volumes over which there is a gap in such solutions (about 40 % for the first gap in figure 2). Since these gaps correspond to parameters for which there is no stable solution, this is a relevant consideration when trying to manufacture glass lenses of given dimensions. The approximation made to the pressure on the upper surface of the drop has little effect on either the drop shape or the solution branches (figures 4 and 5).

We have developed a numerical scheme to determine the linear stability of the static equilibria. This stability problem differs from the classic case of the oscillations of an isolated viscous drop (Reid 1960; Chandrasekhar 1961) in a number of ways: the unperturbed state is non-spherical and only known numerically; the restoring force is determined non-locally due to the lubrication pressure; a vertical translation is not neutrally stable but must be determined by the condition of global vertical-force balance. The numerical predictions are in good agreement with time-dependent simulations. It is found that, depending on the parameters, the onset of instability can

be either direct or oscillatory and can occur either at a fold in the solution branch or before the fold is reached. In all cases investigated, only the lowest-lying (smallest radius) solution could be stable and for some parameters even this was unstable.

The most important features of the solutions for a mould radius $a_M = 50$ are as follows (see figures 6, 7 and 12). For $Ca < 10^{-7}$ there is a continuous branch of stable solutions along the trend of the sessile solution (to at least $Bo = 200$). As Ca increases, gaps open up in this branch so that there are intervals of Bo where there are either no solutions or no stable solutions. As Ca increases further, these gaps grow and merge until by $Ca = 10^{-1}$ there are no stable solutions for $Bo > 12$. The region of stability is largely determined by the existence of a solution close to the sessile trend though there are two regions, around $(Bo, Ca) = (55, 10^{-3})$ and $(130, 10^{-2})$, where such a solution exists but is unstable.

The region of stability limits the lens manufacturing process. The sample parameters in § 1.1 give $Ca = 10^{-6}$, which would prevent manufacture in the range $20 < Bo < 30$ unless some of the parameters could be varied significantly. We tried radial variations in the rate of air injection v (which might be achieved by varying the thickness of the mould), but found that the excluded range of Bo varied little with the injection profile and mainly with the total flux. This reflects the importance of air flow through the final nip at the edge of the drop. By contrast, the excluded range of Bo increases, and the limits to manufacture become more severe, for a mould with larger radius of curvature, as shown in figure 8 and experienced in practice.

We note finally that the complicated behaviour described herein is for the simplest case of a very viscous drop with no inertia and a supporting air cushion fed by a uniform fixed flow. If the drop is less viscous, or if the supporting air cushion is generated by evaporation in the Leidenfrost problem, then the addition of inertia and time-dependent heat transfer is likely to introduce new modes of oscillation and instability.

We are very grateful to E. J. Hinch for helpful discussions on this problem and to the MAGICAL EU grant HPRN-CT-2002-00332 for financial support (L. D. and A. P.).

Appendix. Calculation of the perturbation pressure

Consider a equilibrium drop with parametric shape $\tilde{\boldsymbol{x}}(s) = [\tilde{r}(s), \tilde{z}(s)]$ and outward normal and tangent

$$\boldsymbol{n} = (\tilde{z}', -\tilde{r}'), \qquad \boldsymbol{t} = (\tilde{r}', \tilde{z}'). \tag{A 1}$$

Let the interface be perturbed in the normal direction to $\boldsymbol{x}(s) = \tilde{\boldsymbol{x}}(s) + \delta(s)\boldsymbol{n}(s)$, where $|\delta| \ll 1$. We wish to calculate the linearized perturbation ΔP to the modified pressure (2.8) on the drop.

Though s is the arc length for the unperturbed shape and $\tilde{r}'^2 + \tilde{z}'^2 = 1$, it is not the arc length for the perturbed shape since $(r'^2 + z'^2)^{1/2} \approx 1 + \tilde{\kappa}\delta$. Thus, the perturbed curvature is calculated by linearizing

$$\kappa = \frac{z''r' - r''z'}{(r'^2 + z'^2)^{3/2}} + \frac{z'}{r(r'^2 + z'^2)^{1/2}} \tag{A 2}$$

about $(\tilde{r}, \tilde{z})$ to obtain

$$\Delta\kappa = -\delta'' - \tilde{\kappa}^2\delta - \frac{\tilde{z}'^2\delta}{\tilde{r}^2} - \frac{\tilde{r}'\delta'}{\tilde{r}}. \tag{A 3}$$

The change to the lubrication pressure

$$p = 6Ca \int_{r(s)}^{`\infty'} \frac{r\,\mathrm{d}r}{h^3}, \qquad h(r,z) = z - f(r) \tag{A 4}$$

is most readily evaluated using the decomposition $\boldsymbol{n} = (\tilde{z}'\boldsymbol{t} - \hat{\boldsymbol{z}})/\tilde{r}'$ of the normal into vertical and tangential displacements, since the vertical displacement affects only the integral in (A 4) through its dependence on h and the tangential displacement gives only an end-point contribution at $r(s)$. Thus

$$\frac{\Delta p}{6Ca} = -\int_{r}^{`\infty'} \frac{\delta}{r'}\frac{\partial}{\partial z}\frac{r\,\mathrm{d}r}{h^3} + \frac{\delta z'}{r'}\frac{\mathrm{d}}{\mathrm{d}s}\int_{r(s)}^{`\infty'} \frac{r\,\mathrm{d}r}{h^3} = \int_{s}^{L} \frac{3\delta\, r\,\mathrm{d}s}{h^4} - \left.\frac{\delta\, z' r}{h^3}\right|_{s}. \tag{A 5}$$

Combining these results, we obtain

$$\Delta P = -\tilde{r}'\delta + \Delta\kappa - \frac{6Ca\,\tilde{z}'\tilde{r}\,\delta}{[\tilde{z} - f(\tilde{r})]^3} + 18Ca \int_{s}^{L} \frac{\tilde{r}\,\delta\,\mathrm{d}s}{[\tilde{z} - f(\tilde{r})]^4}, \tag{A 6}$$

where $\Delta\kappa$ is given by (A 3).

REFERENCES

Chandrasekhar, S. 1961 *Hydrodynamic and Hydromagnetic Stability*. Dover.

Duchemin, L., Lister, J. R. & Lange, U. G. 2005 Static shapes of levitated viscous drops. *J. Fluid Mech.* **533**, 161–170.

Goldshtik, M. A., Khanin, V. M. & Ligai, V. G. 1986 A liquid drop on an air cushion as an analogue of Leidenfrost boiling. *J. Fluid Mech.* **166**, 1–20.

Hinch, E. & Lemaitre, J. 1994 The effect of viscosity on the height of disks floating above an air table. *J. Fluid Mech.* **273**, 313–322.

Lange, U. 2002 Gas-film levitation of viscous glass droplets. ECMI Glass Days, Wattens, Austria.

Lee, S. H. & Leal, L. G. 1982 The motion of a sphere in the presence of a deformable interface. *J. Colloid Interface Sci.* **87**, 81–106.

Pozrikidis, C. 1992 *Boundary Integral and Singularity Methods for Linearized Viscous Flow*. Cambridge University Press.

Rallison, J. M. & Acrivos, A. 1978 A numerical study of the deformation and burst of a viscous drop in an extensional flow. *J. Fluid Mech.* **89**, 191–200.

Reid, W. H. 1960 The oscillations of a viscous liquid drop. *Quar. Appl. Math.* **18**, 86–89.

Seward, T. P. & Vascott, T. 2006 *High Temperature Glass Melt Property Database for Process Modeling*. Wiley.

Wilson, S. & Jones, A. 1983 The entry of a falling film into a pool and the air-entrainment problem. *J. Fluid Mech.* **128**, 219–230.